Arabian Journal of Chemistry (2022) **15**, 104092

King Saud University

**Arabian Journal of Chemistry**

www.ksu.edu.sa
www.sciencedirect.com

ORIGINAL ARTICLE

# Electrochemiluminescence biosensor for carcinoembryonic antigen detection based on Au-Ag/g-$C_3N_4$ nanocomposites

**Xiuhua Wei [a], Xing Qiao [b], Jie Fan [a], Hui Dong [a], Yintang Zhang [a], Yanli Zhou [a], Maotian Xu [a,*]**

[a] *Henan Key Laboratory of Biomolecular Recognition and Sensing, College of Chemistry and Chemical Engineering, Henan Joint International Research Laboratory of Chemo/Biosensing and Early Diagnosis of Major Diseases, Shangqiu Normal University, Shangqiu 476000, PR China*
[b] *Central Lab at Zhengzhou First People Hospital, Zhengzhou First People Hospital, Zhengzhou 450000, PR China*

Received 11 April 2022; accepted 30 June 2022
Available online 8 July 2022

**KEYWORDS**

Au-Ag/g-$C_3N_4$;
Electrochemiluminescence;
Carcinoembryonic antigen;
Aptasensor

**Abstract** Herein, an electrochemiluminescence (ECL) aptasensor for carcinoembryonic antigen (CEA) detection was developed based on Au-Ag/g-$C_3N_4$ nanocomposites (NCs), which were synthesized by decorating graphitic carbon nitride (g-$C_3N_4$) nanosheets with alloy-structured Au-Ag bimetallic nanoparticles (NPs) via one-step in situ chemical reduction. As ECL sensing platform, Au-Ag/g-$C_3N_4$ NCs could significantly improve the ECL intensity of luminol due to the good conductivity of Au-Ag NPs, electrocatalytic activity for oxygen evolution reaction (OER) and the ability to adsorb luminol via π stacking interaction. In addition, it could load the thiol terminated aptamers of CEA via Au-S or Ag-S bonds. In the presence of CEA, the ECL response of the proposed biosensor decreased significantly due to the fact that the assembled protein layers hindered the electron transfer and the diffusion of ECL reactants toward the electrode surface. The proposed ECL sensor exhibited a good linear relationship with CEA in the range of 1.0–1.0 × $10^{-6}$ ng/mL with a detection limit of 8.9 × $10^{-7}$ ng/mL. The satisfactory results were obtained in the detection of CEA in human serum samples.

© 2022 The Author(s). Published by Elsevier B.V. on behalf of King Saud University. This is an open access article under the CC BY-NC-ND license (http://creativecommons.org/licenses/by-nc-nd/4.0/).

* Corresponding author at: Henan Key Laboratory of Biomolecular Recognition and Sensing, College of Chemistry and Chemical Engineering, Shangqiu Normal University, Shangqiu, Henan 476000, PR China.
E-mail address: xumaotian@sqnu.edu.cn (M. Xu).

Peer review under responsibility of King Saud University.

Production and hosting by Elsevier

https://doi.org/10.1016/j.arabjc.2022.104092
1878-5352 © 2022 The Author(s). Published by Elsevier B.V. on behalf of King Saud University.
This is an open access article under the CC BY-NC-ND license (http://creativecommons.org/licenses/by-nc-nd/4.0/).

## 1. Introduction

As is known, the early diagnosis is critical for cancer treatment and control. Carcinoembryonic antigen (CEA) is one of the important markers of various tumors (Jie et al., 2011). Therefore, development of a sensitive, rapid and reliable analytical method for CEA detection is important for early diagnosis and therapy of cancers. Numerous detection techniques have been well developed for CEA detection such as electrochemical (Su et al., 2017; Wei et al., 2018; Luo et al., 2018; Mazloum-Ardakani et al., 2019), photoelectrochemical (Song et al., 2017), fluorescent (Lin et al., 2017), electrochemiluminescent (Wang et al., 2015; Liu et al., 2018), surface-enhanced raman scattering (Wang et al., 2017) and colorimetric (Xiao et al., 2017) methods. Specifically, label-free electrochemiluminescence (ECL) biosensors (Zhang et al., 2013a,b; Chen et al., 2014; Liu et al., 2014; Zhang et al., 2017) have been rapidly developed to determine CEA due to its fast response, simple fabrication and high sensitivity.

Label-free sensors require electrode materials with good conductivity and large specific surface area to accelerate electron transfer and immobilize more analytes. Graphitic carbon nitride (g-$C_3N_4$), possesses high nitrogen content with excellent stability (Groenewolt and Antonietti, 2005), low cost, easily tailorable structure and bulk preparation. Recently, g-$C_3N_4$ has been used as an electrocatalyst for oxygen evolution reaction (OER) (Tian et al., 2014; Desalegn et al., 2019). However, the electrocatalytic activity of g-$C_3N_4$ itself is insufficient due to its low specific surface area and poor electronic conductivity. The pyridinic-N atoms in the g-$C_3N_4$ matrix provide rich electron lone pairs, which can capture metal ions in the ligands (Zou et al., 2014). It has been reported that the metal-g-$C_3N_4$ complex could act as a high activity electrocatalyst for OER due to the precise M-$N_2$ coordination (Zheng et al., 2017) and dissolved $O_2$ in electrolyte is a key co-reactant for luminol ECL system (Cui et al., 2003; Wei et al., 2013; Wang et al., 2014; Xia et al., 2022). In addition, it was found that the Au-Ag alloy displayed an effective improvement for luminol ECL in our previous work (Wei et al., 2013; Wang et al., 2014). Therefore, g-$C_3N_4$ nanosheets loaded with bimetallic Au-Ag is expected to be very effective in enhancing luminol ECL intensity.

In this work, considering that the advantages of ECL sensor such as fast response and high sensitivity, an ECL aptasensor for CEA detection based on Au-Ag/g-$C_3N_4$ nanocomposites (NCs) has been constructed. For the ECL sensing platform, the Au-Ag/g-$C_3N_4$ NCs were more favorable for loading the aptamer of CEA via Au-S or Ag-S bond due to the large specific surface area. Meanwhile, the Au-Ag/g-$C_3N_4$ NCs could significantly improve luminol ECL intensity due to the good conductivity of Au-Ag NPs, electrocatalytic performance for OER and the ability to adsorb luminol via π stacking interaction. After CEA interacted specifically with the aptamer, ECL intensity was significantly decreased. Based on this, the proposed lable-free ECL aptasensor was developed and used to detect CEA in human serum samples with satisfactory results.

## 2. Experimental section

### 2.1. Synthesis of Au-Ag/g-$C_3N_4$ NCs

g-$C_3N_4$ nanosheets were first synthesized by urea pyrolysis according to the process described in the literature (Xu et al., 2013). The detailed synthesis procedure was presented in the Electronic Supplementary Material. Au-Ag/g-$C_3N_4$ NCs were prepared according to the method in the literature (Feng et al., 2015) with some modifications. Simply, under stirring, 0.040 mL of 0.1 M $AgNO_3$ and 0.060 mL of 0.1 M $HAuCl_4$ were added to 50 mL of 0.1 mg/mL g-$C_3N_4$ suspension, followed by stirring for 30 min at room temperature. Then, a mixed solution of 0.040 mL 0.08 mM $NaBH_4$ and 0.250 mL 0.5 mM sodium citrate was added rapidly into the boiling suspension and stirred for 15 min. After centrifuging and washing with ultrapure water three times, the Au-Ag/g-$C_3N_4$ NCs were obtained and dispersed in 50 mL ultrapure water.

### 2.2. Fabrication of ECL aptasensor

All glassy carbon electrodes (GCE) were polished with 0.3 and 0.05 μm alumina slurries and followed by ultrasonic cleaning with $HNO_3$ (1:1), ethanol and deionized water in succession. Sequentially, the cleaned electrode was dried with nitrogen. The fabrication process of the ECL sensor was demonstrated in Scheme 1. Firstly, 2 μL Au-Ag/g-$C_3N_4$ NCs was spread on the cleaned and air-dried. Secondly, the modified electrode was incubated in 1.5 μM aptamer at 4 °C overnight, then immersed into 0.1 mM β-mercaptoethanol (β-ME) for 30 min. After careful rinsing and drying, the electrode was incubated in CEA solution for 90 min at 37 °C. Finally, the modified electrode was washed carefully and stored at 4 °C for later use.

The materials, reagents and apparatus required for the experiments and the ECL measurement procedure were presented in the Electronic Supplementary Material. All ECL measurements were performed in 0.1 M PBS (pH = 7.4) containing $5 \times 10^{-5}$ M luminol and $5 \times 10^{-6}$ M $H_2O_2$.

## 3. Results and discussion

### 3.1. Characterization of the Au-Ag/g-$C_3N_4$ NCs

SEM image of the as-prepared g-$C_3N_4$ nanosheets was shown in Fig. 1A. It's clear that g-C3N4 nanosheets were almost transparent thin layer and had many folds, which could facilitate the loading of Au-Ag NPs. TEM image of the Au-Ag/g-C3N4 NCs was shown in Fig. 1B. The spherical Au-Ag NPs of about 4 nm were dispersed uniformly on the surfaces of g-C3N4 nanosheets without any agglomeration, which could be ascribed to a large number of anchoring sites provided by —NH2 and —NH— groups on g-C3N4 nanosheets surfaces (Wang et al., 2016).

The high-resolution TEM (HRTEM) image was shown in Fig. 1C, which exhibited a polycrystalline microstructure of the metal NPs (Zhang et al., 2013a,b). As displayed in Fig. 1D (enlarged from the red circle region of Fig. 1C), a high-resolution lattice fringe of 0.24 nm was observed, which ascribed to the (1 1 1) lattice planes of crystalline Au or Ag. The polycrystalline nature was also identified by selected-area electron diffraction (SAED) analysis. As displayed in the inset in Fig. 1C, the four diffraction rings were indexed to the (3 1 1), (2 2 0), (2 0 0) and (1 1 1) Bragg reflections from the face-centered cubic structure of Au or Ag, suggesting the polycrystalline nature of metal NPs (Sun et al., 2018).

Compared with g-C3N4 nanosheets, the obtained Au-Ag/g-C3N4 NCs had a larger specific surface area (Fig. 2A), which was beneficial to the loading of biological molecules. The elemental distribution of Au-Ag/g-C3N4 NCs was investigated by energy dispersive X-ray spectroscopy (EDS). As presented in Fig. 2B–E, C, N, Au and Ag were uniformly distributed throughout the whole materials. The EDS spectrum in Fig. 2F further confirmed that the resulting nanocomposites based on the g-C3N4 nanosheets incorporating with two

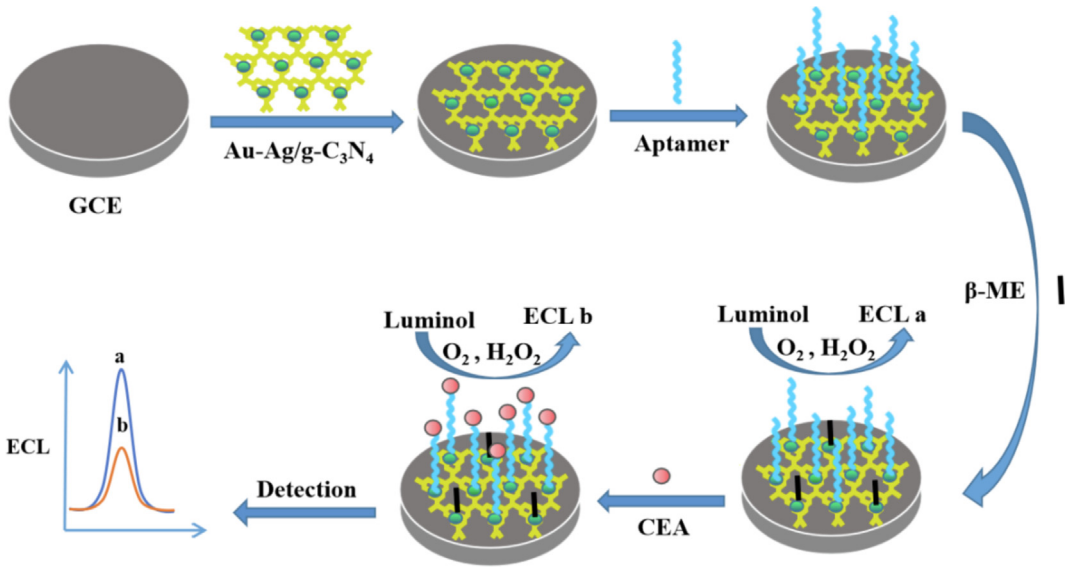


**Scheme 1** Fabrication process of the ECL aptasensor.

metals had been successfully assembled. Moreover, the resulting nanocomposites was characterized by XRD. As shown in Fig. 2G, a weak characteristic diffraction peak of g-C3N4 was observed at 27.45°, which is assigned to the (002) crystal plane and associated with the interlayer stacking of aromatic segments (Chen et al., 2014).

In order to investigate the components of the obtained nanocomposites, XPS measurement was performed. The existence of C, N, Au and Ag elements was further verified by the survey XPS spectrum shown in Fig. 3A, while O element was also detected, indicating the formation of oxygen-containing functional groups. As shown in Fig. 3B, the binding energies of Au $4f_{7/2}$ (83.0 eV) and Au $4f_{5/2}$ (86.7 eV) were lower than that of bulk Au(0) nanocrystals (83.7 eV for Au $4f_{7/2}$ and 87.7 eV for Au $4f_{5/2}$) (Luo et al., 2012), suggesting that the Au atoms were negatively charged. As shown in Fig. 3C, the binding energies of Ag $3d_{5/2}$ (367.8 eV) and Ag $3d_{3/2}$ (373.8 eV) were between that of Ag(1) complexes (366.8 eV and 372.8 eV) and neutral bulk Ag(0) (368.2 eV and 374.2 eV) (Mao et al., 2016), indicating that the Ag atoms were positively charged. In addition, the diffraction peaks for $Ag_2O$ (JCPDS 41–1104) were not presented in the XRD pattern (Fig. 2G), suggesting that there was no $Ag_2O$ in the Au-Ag/g-$C_3N_4$ NCs. The above results indicated that charge transfer occurred from Ag (electronegativity = 1.93) to Au (electronegativity = 2.54). Thus, the positively charged Ag atoms and the negatively charged Au atoms were chemically bonded to form Au-Ag NPs (Negishi et al., 2010).

As shown in Fig. 3D, the UV–Vis spectra also revealed the bimetallic alloy-structure information. Apart from the characteristic absorption band of g-$C_3N_4$ at 330 nm, the UV–vis spectra of Au-Ag/g-$C_3N_4$ NCs did not show two independent absorption bands (397 nm for Ag NPs and 520 nm for Au NPs) but a single band of 509 nm attributed to the blue shift of the characteristic peak of Au NPs, further confirming the formation of Au-Ag nanoalloys (Sobczak and Dembowiak, 2015; Sun et al., 2018).

### *3.2. Construction and characterization of the ECL aptasensor*

To investigate the effects of Au-Ag/g-$C_3N_4$ NCs on the ECL intensity of luminol, the ECL responses on GCE modified respectively with Au-Ag/g-$C_3N_4$ NCs, Au/g-$C_3N_4$, Ag/g-$C_3N_4$, Au-Ag NPs and g-$C_3N_4$ nanosheets were shown in Fig. 4A. The classic mechanism ECL mechanism for luminol-$O_2$ (or $H_2O_2$) system at the anode was that luminol anion ($LH^-$) was electrochemically oxidized into luminol anion radical ($L^{\bullet -}$) at positive potential (Fig. 4B), followed by further oxidation by dissolved $O_2$ or $H_2O_2$ into an excited state luminophore ($AP^{2-*}$) (Xia et al., 2022). Obviously, the dissolved $O_2$ is a key co-reactant for luminol ECL system (Cui et al., 2003; Wei et al., 2013; Wang et al., 2014; Xia et al., 2022). The GCE modified with g-$C_3N_4$ nanosheets exhibited stronger ECL intensity than the bare GCE, which could be attributed to the electrocatalytic activity for OER ($4OH^- - 4e^- = 2H_2O + O_2$) (Tian et al., 2014; Desalegn et al., 2019). The previous literature reported that Au, Ag or Au-Ag alloy could significantly improve ECL intensity of luminol due to its excellent electronic conductivity and catalytic performance for luminol ECL reaction (Wei et al., 2013; Wang et al., 2014). The GCE modified with Au/g-$C_3N_4$, Ag/g-$C_3N_4$ or Au-Ag/g-$C_3N_4$ showed stronger ECL intensity than that of the GCE modified with Au-Ag NPs or g-$C_3N_4$ nanosheets. Moreover, the GCE modified with Au-Ag/g-$C_3N_4$ exhibited the strongest ECL intensity. Thus, there was a synergistic effect between metal NPs and g-$C_3N_4$ nanosheets. The good strengthening performance of Au-Ag/g-$C_3N_4$ NCs for luminol ECL could be attributed to not only the good conductivity due to Au-Ag NPs but also the good electrocatalytic activity for OER (Fig. 4B). In addition, luminol could be absorbed on the modified electrode surface via π stacking interaction between the aromatic rings of luminol and the conjugated π-systems of g-$C_3N_4$, which also favored the ECL reaction of luminol.

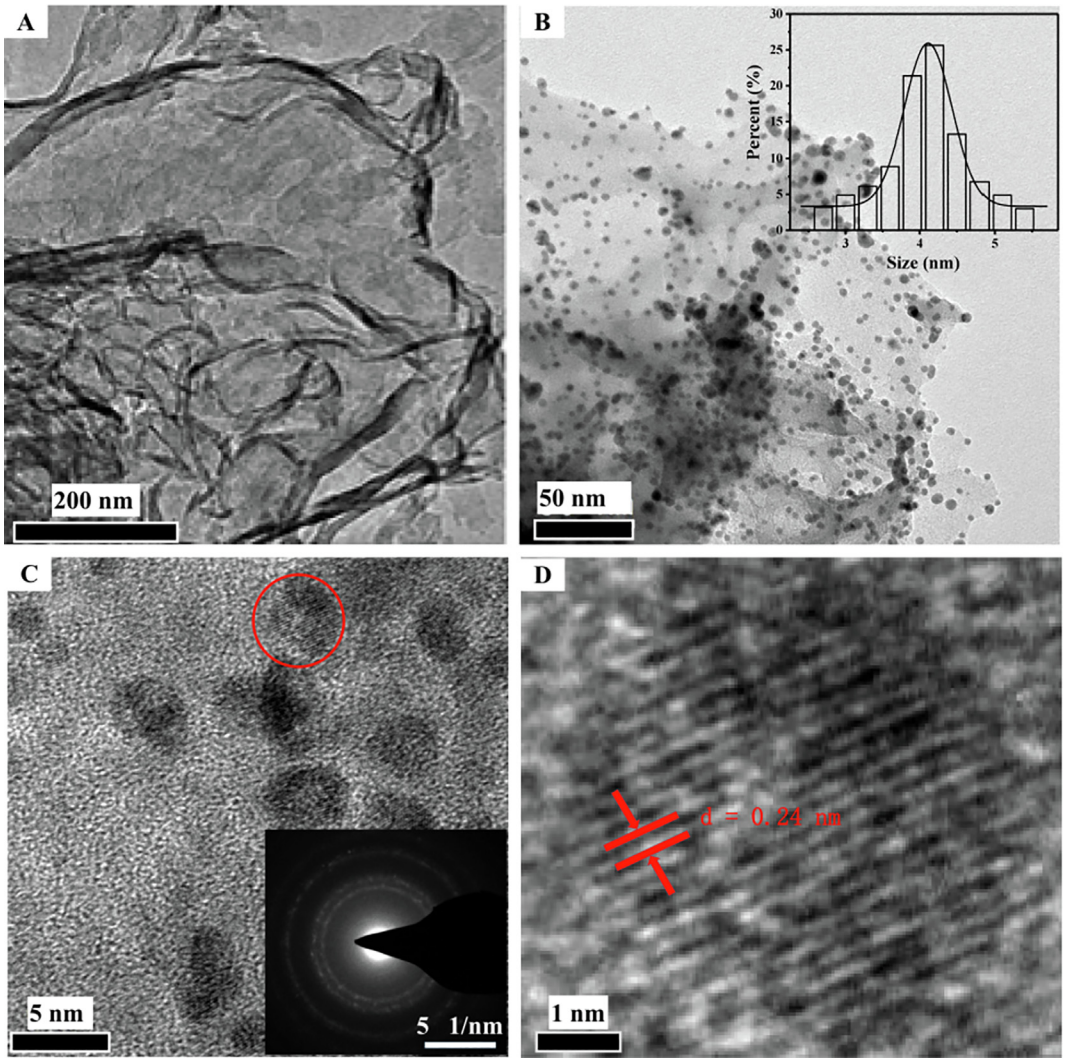


**Fig. 1** (A) SEM image of g-$C_3N_4$ nanosheets. (B) TEM image. Inset: corresponding particle size distribution of the Au-Ag NPs, (C) HRTEM image (inset SAED image) and (D) HRTEM image enlarged from the red circle region in Fig. 1C of the obtained Au-Ag/g-$C_3N_4$ NCs.

In view of the good strengthening performance for luminol ECL Au-Ag/g-$C_3N_4$ NCs were used as the ECL sensing platform for CEA detection. The thiol terminated CEA aptamers were covalently bound to the Au-Ag NPs surface via Au-S or Ag-S bonds. After the nonspecific binding sites were blocked with β-mercaptoethanol, the aptasensor was incubated in CEA-containing solution for CEA detection. The ECL signals at different assembly stages of the proposed aptasensor were recorded to monitor the fabrication processes. As shown in Fig. 4C, after aptamer, β-ME and CEA were assembled onto the GCE modified with Au-Ag/g-$C_3N_4$ NCs, the ECL signal decreased sequentially because the assembled protein layers hindered the electron transfer of ECL reaction and the diffusion of ECL reactants toward the electrode surface (Chen et al., 2014). Based on above results, an ECL aptasensor was successfully constructed for CEA detection.

Furthermore, the interface property change of the modified electrode surface was monitored by electrochemical impedance spectroscopy (EIS). Compared to the bare GCE, the lower charge transfer resistance ($R_{ct}$) of the Au-Ag/g-$C_3N_4$/GCE was attributed to the good conductivity of Au-Ag/g-$C_3N_4$ NCs. The $R_{ct}$ increased significantly after the assembly of aptamer, β-mercaptoethanol and CEA in sequence (Fig. 4D), which could be attributed to the poor conductivity of the assembled layers. Meanwhile, the cyclic voltammetry (CV) results shown in Fig. 4E was consistent with the EIS results.

### *3.3. Optimization of experimental conditions*

For improving the analytical performance of the aptasensor, the experimental conditions have been optimized in detail. As shown in Fig. 5A, the optimal molar ratio of Au to Ag was 3:2. When the concentration of g-$C_3N_4$ was 0.1 mg/mL, the ECL intensity reached the maximum (Fig. 5B). The coated volume of Au-Ag/-g-$C_3N_4$ NCs was optimized as approximately 2 μL (Fig. 5C). As shown in Fig. 5D, ΔECL (the decrease in ECL intensity) increased with increasing aptamer concentrations, while became very slow after 1.5 μM. The effects of incubation time and luminol concentration on ΔECL

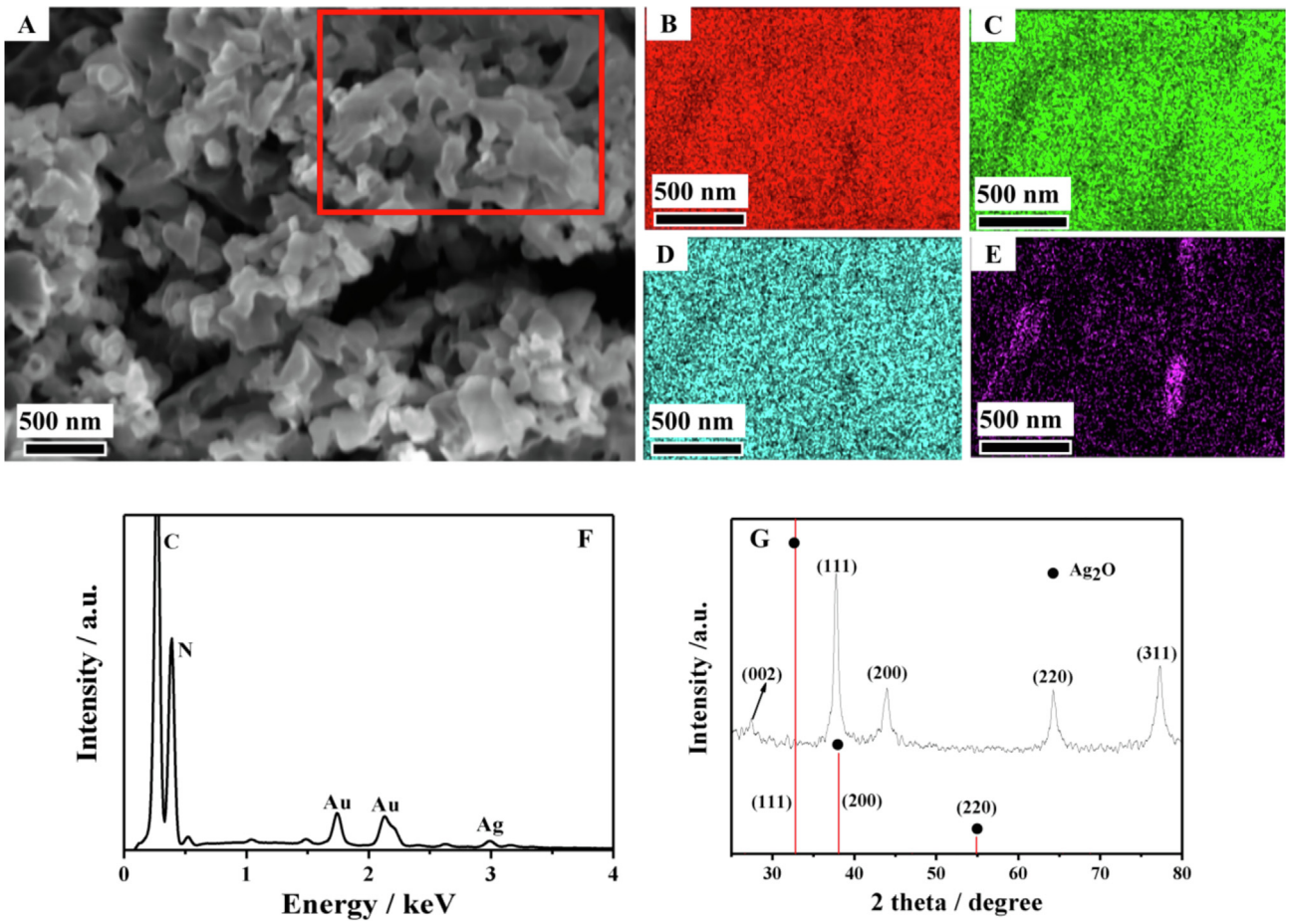


**Fig. 2** SEM image (A), element mapping images (from the red rectangle region in Fig. 2A) of C, N, Ag, Au (B–E), EDS spectrum (F) and XRD pattern (G) of the obtained Au-Ag/g-$C_3N_4$ NCs.

were also investigated. The ΔECL were almost unchanged after 90 min (Fig. 5E) and $5 \times 10^{-5}$ M luminol concentration (Fig. 5F). Therefore, 1.5 μM aptamer concentration, incubation time of 90 min and $5 \times 10^{-5}$ M luminol concentration were selected for subsequent experiments.

In addition, the selection of $H_2O_2$ concentration was based on two aspects. On the one hand, the ECL intensity of luminol in PBS (pH = 7.4) containing dissolved $O_2$ was too weak to be used as background signal for the detection of CEA. Thence, $H_2O_2$ was chosen to enhance the ECL intensity of luminol. On the other hand, $H_2O_2$ would decompose in PBS (pH = 7.4), the concentration should be kept as low as possible. Considering the above two aspects, the concentration of $H_2O_2$ selected in this experiment was $5 \times 10^{-6}$ M.

### *3.4. Analytical performance of the ECL aptasensor*

The property of the developed ECL aptasensor was investigated under the optimum conditions. As exhibited in Fig. 6A, with the increase of CEA concentration, the ECL peak intensity weakened. A linear regression of ΔI (ΔI as the decreased ECL peak intensity after incubation with CEA) upon the $\log C_{CEA}$ was established in the range of $1.0 \times 10^{-6}$ ng/mL to 1.0 ng/mL with a regression equation of $\Delta I = 816 + 67.6 \log C_{CEA}$ ($R^2 = 0.992$). The detection limit of $8.9 \times 10^{-7}$ ng/mL (S/N = 3) was lower than that reported in the literatures listed in Table S1. The excellent signal stability of the ECL aptasensor for $1.0 \times 10^{-2}$ ng/mL CEA in 600 s was demonstrated in the inset of Fig. 6B.

### *3.5. Reproducibility, stability and specificity of the ECL aptasensor*

In Fig. 7A, the reproducibility of the developed aptasensor was researched by detecting the CEA (0.1 ng/mL) using the four different prepared aptasensors under the same condition and the RSD (n = 4) was 3.8%, indicating the proposed aptasensor had good reproducibility.

The long-term stability of the prepared ECL aptasensor was also investigated. After the prepared aptasensor was stored at 4 °C for one month, the original signal decreased by 5.5%, indicating the proposed sensor had a good stability.

Moreover, to examine the specificity of the proposed aptasensor, the responses of the proposed aptasensor for other interferences were measured. The concentration of the CEA and the interferences was all 1.0 ng/mL. As displayed in Fig. 7B, the ECL signal of CEA was significantly lower than that of other interfering substances, indicating the proposed

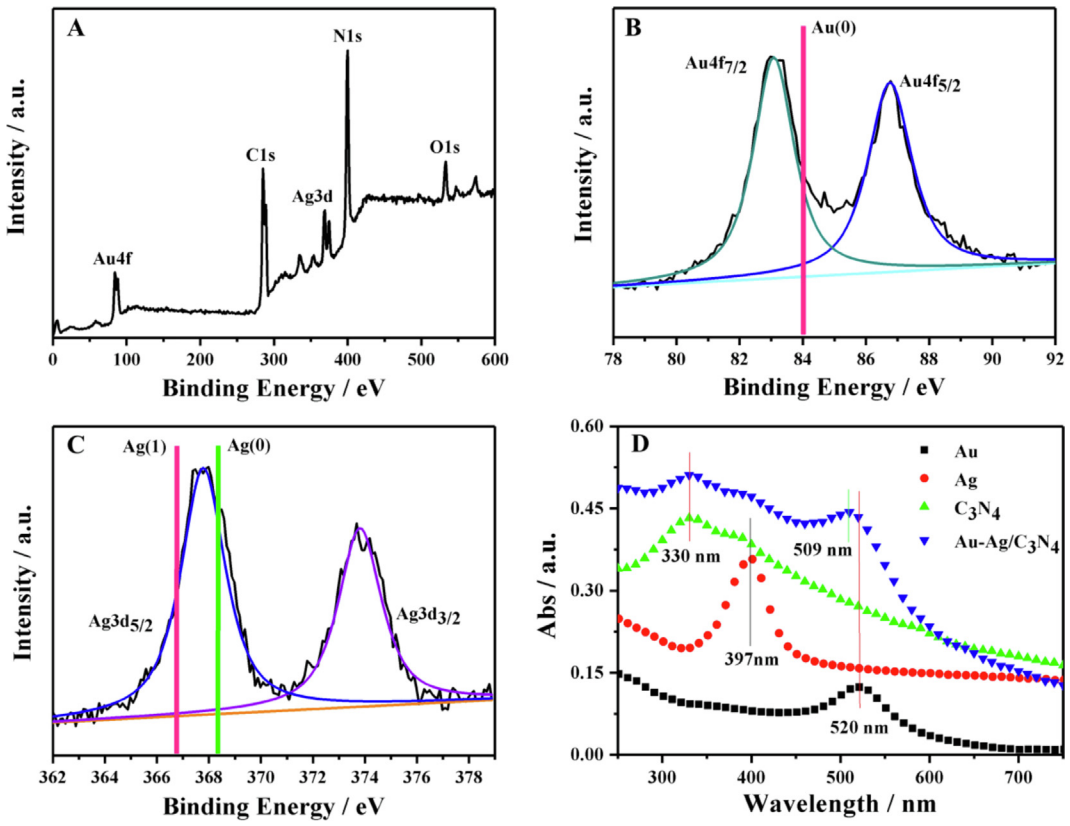


**Fig. 3** XPS spectra of the obtained Au-Ag/g-$C_3N_4$ NCs: (A) survey spectra, (B) Au 4f spectra and (C) Ag 3d spectra. The red line in (B) represents Au $4f_{7/2}$ in the Au (0) film, the red line and the green line in (C) represent Ag $3d_{5/2}$ in the Ag (1) complexes and Ag (0) film respectively. (D) UV–vis absorption spectra of the as-prepared Au, Ag, g-$C_3N_4$, and Au-Ag/g-$C_3N_4$ NCs.

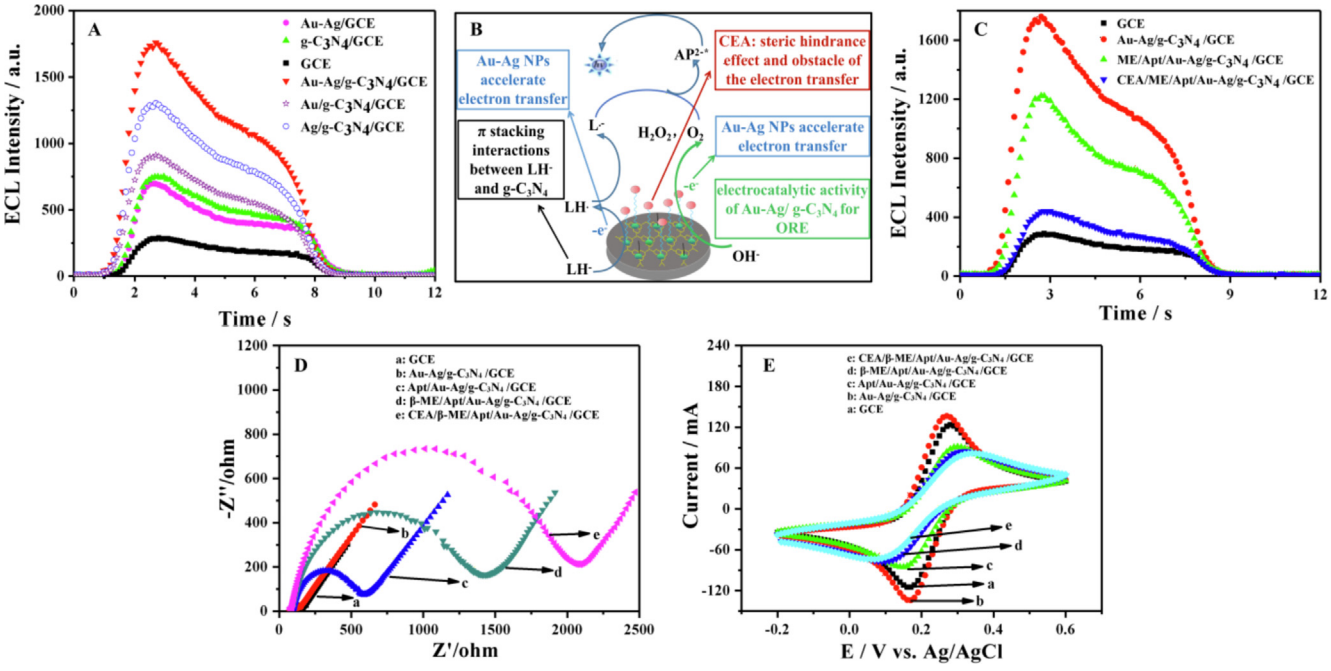


**Fig. 4** (A) Influence of the different nanomaterials on ECL intensity. (B) The possible ECL mechanisms of the proposed aptasensor. (C) ECL responses at the different fabrication stages of the aptasensor (1.0 ng/mL CEA). (D) EIS and (E) CV of the different modified electrodes in 5.0 mM $[Fe(CN)_6]^{3-/4-}$ containing 0.1 M KCl.

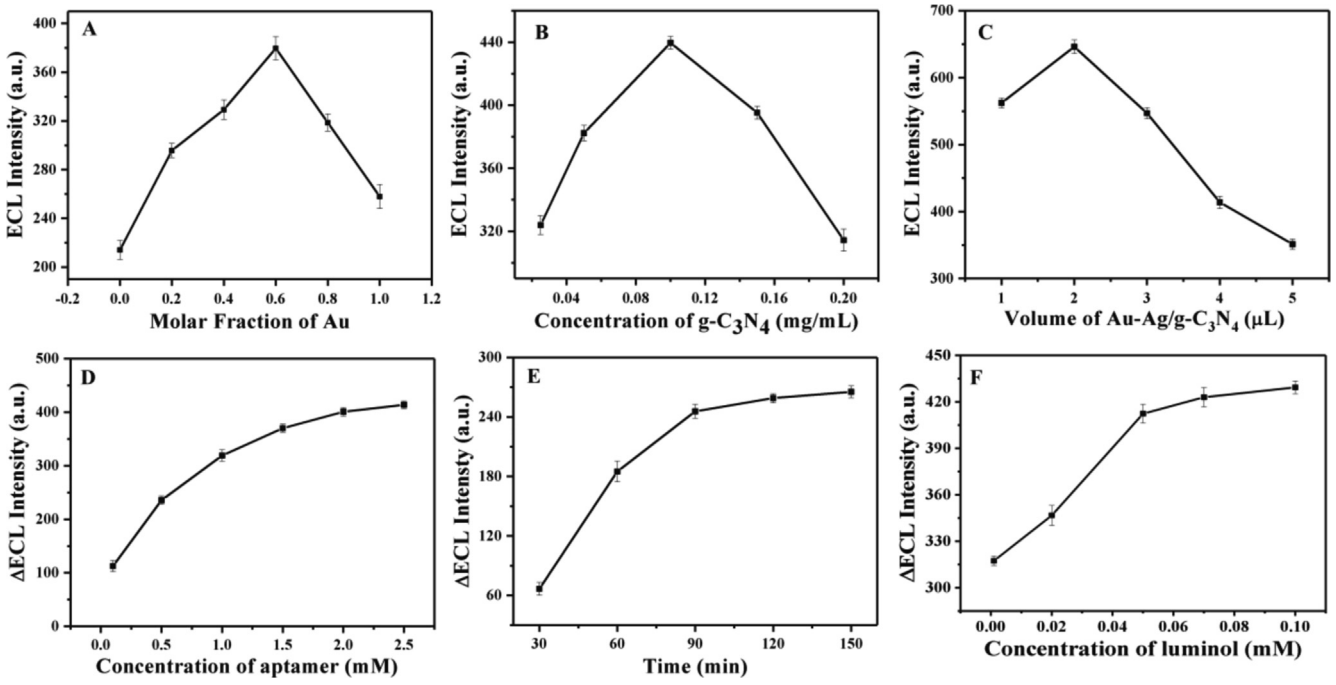


**Fig. 5** Effects of Au molar fraction in Au-Ag NPs (A), g-$C_3N_4$ concentration (B), drip volume of Au-Ag/g-$C_3N_4$ NCs (C), aptamer concentration (D), incubation time in $1.0 \times 10^{-6}$ ng/mL CEA (E) and luminol concentration (F) on ECL response.

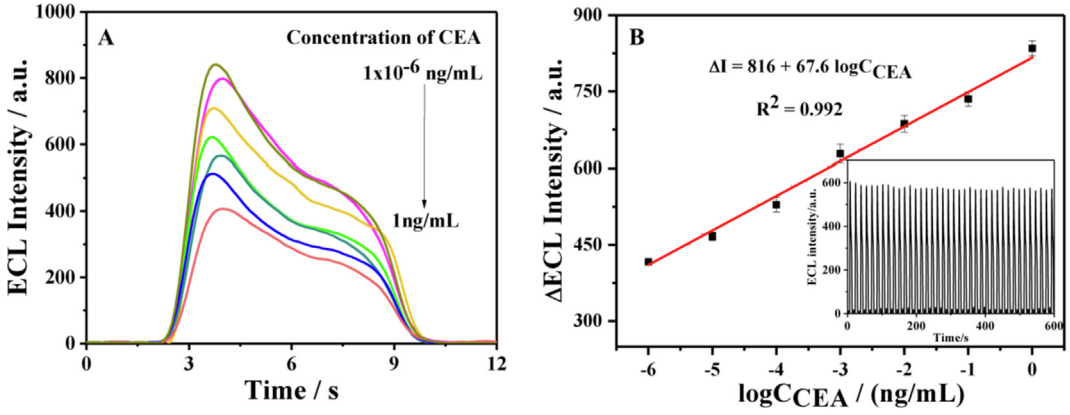


**Fig. 6** (A) The ECL of the aptasensor from different CEA concentration and (B) Linear relationship of ΔECL with $\log C_{CEA}$ (inset: the ECL intensity obtained from $1.0 \times 10^{-2}$ ng/mL CEA for 600 s).

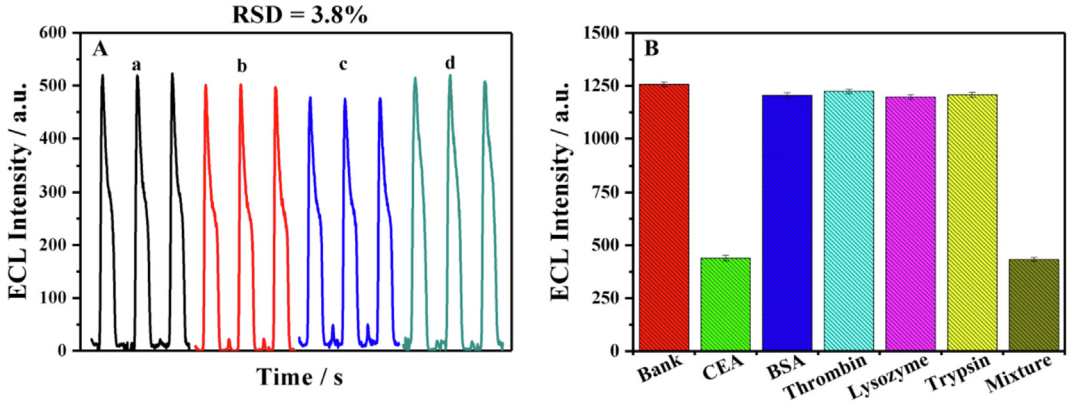


**Fig. 7** (A) The ECL signals from the four prepared ECL aptasensors for 0.1 ng/mL CEA and (B) the ECL responses of the developed aptasensor after incubating with 1.0 ng/mL CEA, BSA, Thrombin, Trypsin and Lysozyme.

**Table 1** Recovery tests for CEA in human serum samples with the proposed aptasensor.

| samples | Added (ng/mL) | Detected (ng/mL) | Found (ng/mL) | RSD% (n = 3) | Recovery (%) |
|---|---|---|---|---|---|
| | 0.00 | 5.06 | – | 3.1 | – |
| 1 | 5.00 | 9.90 | 4.84 | 2.7 | 96.8 |
| | 10.00 | 14.86 | 9.80 | 2.0 | 98.0 |
| | 0.00 | 20.53 | – | 1.8 | – |
| 2 | 20.00 | 41.56 | 21.03 | 2.6 | 105 |
| | 40.00 | 59.36 | 38.83 | 3.5 | 97.1 |

**Table 2** Comparison of CEA concentrations detected by two methods.

| samples | ELISA (ng/mL) | aptasensor (ng/mL) | Error value (ng/mL) |
|---|---|---|---|
| 1 | 0.97 | 1.08 | 0.11 |
| 2 | 5.31 | 5.06 | −0.25 |
| 3 | 20.06 | 20.53 | 0.47 |

aptasensor can specifically recognize CEA with good selectivity, which was expected to be applied to complex biological environments.

### *3.6. Detection of CEA in real samples*

The developed aptasensor was applied to CEA analysis in human serum samples. Considering that the linear range of the aptasensor is lower than the CEA concentration of serum samples, the samples were diluted 1000 times before detected. As presented in Table 1, the recovery rates with the developed aptasensor varied from 96.8% to 105%. In order to verify the accuracy of the developed method, the results determined by the proposed assay had been compared with those obtained by enzyme-linked immunosorbent assay (ELISA) used in hospital (Table 2). The CEA levels detected by the proposed aptasensor were in good agreement with the results detected by ELISA, suggesting the developed ECL aptasensor had great clinical application prospects.

## 4. Conclusions

The Au-Ag/g-$C_3N_4$ NCs was synthesized by decorating g-$C_3N_4$ nanosheets with alloy-structured Au-Ag bimetallic NPs via one-step in situ chemical reduction. As ECL sensing platform, Au-Ag/g-$C_3N_4$ NCs could increase the ECL intensity of luminol due to the electrocatalytic activity for OER, the good electronic conductivity and the ability to adsorb luminol via π stacking interaction. The proposed aptasensor demonstrated a wide linear range with a low detection limit for CEA detection and displayed the results consistent with ELISA for the detection of CEA in human serum samples. This aptasensor could offer a reliable method for the detection of CEA in clinical application.

## Declaration of Competing Interest

The authors declare that they have no known competing financial interests or personal relationships that could have appeared to influence the work reported in this paper.

## Acknowledgments

This research was supported by the National Natural Science Foundation of China (Grant Nos. 22074089 and 21505091) and Henan Province Foundation for University Key Teacher (Grant No. 2018GGJS133).

## Appendix A. Supplementary material

Supplementary data to this article can be found online at https://doi.org/10.1016/j.arabjc.2022.104092.

## References

Chen, L., Zeng, X., Si, P., Chen, Y., Chi, Y., Kim, D.H., Chen, G., 2014. Gold nanoparticle-graphite-like $C_3N_4$ nanosheet nanohybrids used for electrochemiluminescent immunosensor. Anal. Chem. 86, 4188–4195. https://doi.org/10.1021/ac403635f.

Cui, H., Zou, G.Z., Lin, X.Q., 2003. Electrochemiluminescence of luminol in alkaline solution at a paraffin-impregnated graphite electrode. Anal. Chem. 75, 324–331. https://doi.org/10.1021/ac0201631.

Desalegn, B.Z., Jadhav, H.S., Seo, J.G., 2019. Highly efficient g-$C_3N_4$ nanorods with dual active sites as an electrocatalyst for the oxygen evolution reaction. ChemCatChem 11, 2870–2878. https://doi.org/10.1002/cctc.201900330.

Feng, Q., Shen, Y., Li, M., Zhang, Z., Zhao, W., Xu, J., Chen, H., 2015. Dual-wavelength electrochemiluminescence ratiometry based on resonance energy transfer between Au nanoparticles functionalized g-$C_3N_4$ nanosheet and $Ru(bpy)_3^{2+}$ for microRNA detection. Anal. Chem. 88, 937–944. https://doi.org/10.1021/acs.analchem.5b03670.

Groenewolt, M., Antonietti, M., 2005. Synthesis of g-$C_3N_4$ nanoparticles in mesoporous silica host matrices. Adv. Mater. 17, 1789–1792. https://doi.org/10.1002/adma.200401756.

Jie, G., Wang, L., Zhang, S., 2011. Magnetic electrochemiluminescent $Fe_3O_4$/CdSe–CdS nanoparticle/polyelectrolyte nanocomposite for highly efficient immunosensing of a cancer biomarker. Chem. Eur. J. 17, 641–648. https://doi.org/10.1002/chem.201001128.

Lin, Z., Lv, S., Zhang, K., Tang, D., 2017. Optical transformation of a CdTe quantum dot-based paper sensor for a visual fluorescence immunoassay induced by dissolved silver ions. J. Mater. Chem. B 5, 826–833. https://doi.org/10.1039/C6TB03042D.

Liu, F., Cao, J., Wang, Y., Fu, X., Ren, S., Liu, Y., 2018. A spatial-resolved electrochemiluminescence aptasensor for carcinoembryonic antigen detection in a double-check mode. Sensor. Actuat. B-Chem. 276, 173–179. https://doi.org/10.1016/j.snb.2018.08.082.

Liu, M., Ye, Y., Yao, C., Zhao, W., Huang, X., 2014. $Mn^{2+}$-doped $NaYF_4$:Yb/Er upconversion nanoparticles with amplified electrogenerated chemiluminescence for tumor biomarker detection. J. Mater. Chem. B 2, 6626–6633. https://doi.org/10.1039/C4TB00717D.

Luo, Y., Wang, Y., Yan, H., Wu, Y., Zhu, C., Du, D., Lin, Y., 2018. SWCNTs@GQDs composites as nanocarriers for enzyme-free dual-signal amplification electrochemical immunoassay of cancer biomarker. Anal. Chim. Acta 1042, 44–51. https://doi.org/10.1016/j.aca.2018.08.023.

Luo, Z., Yuan, X., Yu, Y., Zhang, Q., Leong, D.T., Lee, J.Y., Xie, J., 2012. From aggregation-induced emission of Au(I)-thiolate complexes to ultrabright Au(0)@Au(I)-thiolate core-shell nanoclusters. J. Am. Chem. Soc. 134, 16662–16670. https://doi.org/10.1021/ja306199p.

Mao, Y., Yang, Y., Yang, H., Han, J., Zeng, Y., Wei, J., Meng, X., Wang, C., 2016. Fabrication and characterization of hierarchical multipod silver citrate complex microcrystals with excellent SERS properties. RSC Adv. 6, 12311–12314. https://doi.org/10.1039/C6RA00221H.

Mazloum-Ardakani, M., Tavakolian-Ardakani, Z., Sahraei, N., Moshtaghioun, S.M., 2019. Fabrication of an ultrasensitive and selective electrochemical aptasensor to detect carcinoembryonic antigen by using a new nanocomposite. Biosens. Bioelectron. 129, 1–6. https://doi.org/10.1016/j.bios.2018.12.047.

Negishi, Y., Iwai, T., Ide, M., 2010. Continuous modulation of electronic structure of stable thiolate-protected Au25 cluster by Ag doping. Chem. Commun. 46, 4713–4715. https://doi.org/10.1039/C0CC01021A.

Sobczak, I., Dembowiak, E., 2015. The effect of AuAg–MCF and AuAg–NbMCF catalysts pretreatment on the gold–silver alloy formation and the catalytic behavior in selective methanol oxidation with oxygen. J. Mol. Catal. A-Chem. 409, 137–148. https://doi.org/10.1016/j.molcata.2015.08.017.

Song, J., Wu, S., Yang, X., Yuan, J., 2017. A carboxylated graphene nanodisks/glucose oxidase nanotags and Mn:CdS/$TiO_2$ matrix based dual signal amplification strategy for ultrasensitive photoelectrochemical detection of tumor markers. Analyst 142, 4647–4654. https://doi.org/10.1039/C7AN01453H.

Su, S., Han, X., Lu, Z., Liu, W., Zhu, D., Chao, J., Fan, C., Wang, L., Song, S., Weng, L., Wang, L., 2017. Facile synthesis of a $MoS_2$–prussian blue nanocube nanohybrid-based electrochemical sensing platform for hydrogen peroxide and carcinoembryonic antigen detection. ACS Appl. Mater. Inter. 9, 12773–12781. https://doi.org/10.1021/acsami.7b01141.

Sun, L., Yin, Y., Wang, F., Su, W., Zhang, L., 2018. Facile one-pot green synthesis of Au–Ag alloy nanoparticles using sucrose and their composition-dependent photocatalytic activity for the reduction of 4-nitrophenol. Dalton Trans. 47, 4315–4324. https://doi.org/10.1039/C7DT03850J.

Tian, J., Liu, Q., Asiri, A.M., Alamry, K.A., Sun, X., 2014. Ultrathin graphitic $C_3N_4$ nanosheets/graphene composites: efficient organic electrocatalyst for oxygen evolution reaction. ChemSusChem 7, 2125–2130. https://doi.org/10.1002/cssc.201402118.

Wang, Y., Hao, N., Feng, Q., Shi, H., Xu, J., Chen, H., 2016. A ratiometric electrochemiluminescence detection for cancer cells using g-$C_3N_4$ nanosheets and Ag–PAMAM–luminol nanocomposites. Biosens. Bioelectron. 77, 76–82. https://doi.org/10.1016/j.bios.2015.08.057.

Wang, D., Li, Y., Lin, Z., Qiu, B., Guo, L., 2015. Surface-enhanced electrochemiluminescence of Ru@$SiO_2$ for ultrasensitive detection of carcinoembryonic antigen. Anal. Chem. 87, 5966–5972. https://doi.org/10.1021/acs.analchem.5b01038.

Wang, K., Wei, X., Tu, Y., 2014. Strong enhancement of the electrochemiluminescence of luminol by AuAg and PtAg alloy nanoclusters, and its sensitization by phenolic artificial oestrogens. Microchim. Acta 181, 1223–1230. https://doi.org/10.1007/s00604-014-1224-7.

Wang, Z., Zong, S., Wu, L., Zhu, D., Cui, Y., 2017. SERS-activated platforms for immunoassay: probes, encoding methods, and applications. Chem. Rev. 117, 7910–7963. https://doi.org/10.1021/acs.chemrev.7b00027.

Wei, Y., Ma, H., Ren, X., Ding, C., Wang, H., Sun, X., Du, B., Zhang, Y., Wei, Q., 2018. A dual-signaling electrochemical ratiometric method for sensitive detection of carcinoembryonic antigen based on Au-$Cu_2S$-CuS/graphene and Au-$CeO_2$ supported toluidine blue complex. Sensor. Actuat. B-Chem. 256, 504–511. https://doi.org/10.1016/j.snb.2017.10.136.

Wei, X., Xiao, C., Wang, K., Tu, Y., 2013. A nano-$TiO_2$ supported AuAg alloy nanocluster functionalized electrode for sensitizing the electrochemiluminescent analysis. J. Electroanal. Chem. 702, 37–44. https://doi.org/10.1016/j.jelechem.2013.05.009.

Xia, H., Zheng, X., Li, J., Wang, L., Xue, Y., Peng, C., Han, Y., Wang, Y., Guo, S., Wang, J., Wang, E., 2022. Identifying luminol electrochemiluminescence at the cathode via single-atom catalysts tuned oxygen reduction reaction. J. Am. Chem. Soc. 144, 7741–7749. https://doi.org/10.1021/jacs.2c00865.

Xiao, L., Zhu, A., Xu, Q., Chen, Y., Xu, J., Weng, J., 2017. Colorimetric biosensor for detection of Cancer biomarker by Au nanoparticle-decorated $Bi_2Se_3$ nanosheets. ACS Appl. Mater. Inter. 9, 6931–6940. https://doi.org/10.1021/acsami.6b15750.

Xu, J., Li, Y., Peng, S., Lu, G., Li, S., 2013. Eosin Y-sensitized graphitic carbon nitride fabricated by heating urea for visible light photocatalytic hydrogen evolution: the effect of the pyrolysis temperature of urea. PCCP 15, 7657–7665. https://doi.org/10.1039/c3cp44687e.

Zhang, G., Du, M., Li, Q., Li, X., Huang, J., Jiang, X., Sun, D., 2013b. Green synthesis of Au–Ag alloy nanoparticles using cacumen platycladi extract. RSC Adv. 3, 1878–1884. https://doi.org/10.1039/C2RA22442A.

Zhang, A., Huang, C., Shi, H., Guo, W., Zhang, X., Xiang, H., Jia, T., Miao, F., Jia, N., 2017. Electrochemiluminescence immunosensor for sensitive determination of tumor biomarker CEA based on multifunctionalized flower-like Au@BSA nanoparticles. Sensor. Actuat. B-Chem. 238, 24–31. https://doi.org/10.1016/j.snb.2016.07.009.

Zhang, Y., Liu, W., Ge, S., Yan, M., Wang, S., Yu, J., Li, N., Song, X., 2013a. Multiplexed sandwich immunoassays using flow-injection electrochemiluminescence with designed substrate spatial-resolved technique for detection of tumor markers. Biosens. Bioelectron. 41, 684–690. https://doi.org/10.1016/j.bios.2012.09.044.

Zheng, Y., Jiao, Y., Zhu, Y., Cai, Q., Vasileff, A., Li, L.H., Han, Y., Chen, Y., Qiao, S.Z., 2017. Molecule-level g-$C_3N_4$ coordinated transition metals as a new class of electrocatalysts for oxygen electrode reactions. J. Am. Chem. Soc. 139, 3336–3339. https://doi.org/10.1021/jacs.6b13100.

Zou, X., Huang, X., Goswami, A., Silva, R., Sathe, B.R., Mikmeková, E., Asefa, T., 2014. Cobalt-embedded nitrogen-rich carbon nanotubes efficiently catalyze hydrogen evolution reaction at all pH values. Angew. Chem. Int. Ed. 53, 4372–4376. https://doi.org/10.1002/anie.201311111.